A ^{17}O Paramagnetic NMR Study of Sm$_2$O$_3$, Eu$_2$O$_3$, and Sm/Eu-substituted CeO$_2$

Michael A. Hope,[1] David M. Halat,[1,2] Jeongjae Lee,[1] Clare P. Grey[1]

1. Department of Chemistry, University of Cambridge, Lensfield Rd, Cambridge CB2 1EW (UK)
2. Department of Chemical and Biomolecular Engineering, University of California, Berkeley, CA 94720, United States.

Abstract

Paramagnetic solid-state NMR of lanthanide (*Ln*) containing materials can be challenging due to the high electron spin states possible for the *Ln f* electrons, which result in large paramagnetic shifts, and these difficulties are compounded for ^{17}O due to the low natural abundance and quadrupolar character. In this work, we present examples of ^{17}O NMR experiments for lanthanide oxides and strategies to overcome these difficulties. In particular, we record and assign the ^{17}O NMR spectra of monoclinic Sm$_2$O$_3$ and Eu$_2$O$_3$ for the first time, as well as performing density functional theory (DFT) calculations to gain further insight into the spectra. The temperature dependence of the Sm^{3+} and Eu^{3+} magnetic susceptibilities are investigated by measuring the ^{17}O shift of the cubic sesquioxides over a wide temperature range, which reveal non-Curie temperature dependence due to the presence of low-lying electronic states. This behaviour is reproduced by calculating the electron spin as a function of temperature, yielding shifts which agree well with the experimental values. Using the understanding of the magnetic behaviour gained from the sesquioxides, we then explore the local oxygen environments in 15 at% Sm- and Eu-substituted CeO$_2$, with the ^{17}O NMR spectrum exhibiting signals due to environments with zero, one and two nearest neighbour *Ln* ions, as well as further splitting due to oxygen vacancies. Finally, we extract an activation energy for oxygen vacancy motion in these systems of 0.35 ± 0.02 eV from the Arrhenius temperature dependence of the ^{17}O T_1 relaxation constants, which is found to be independent of the *Ln* ion within error. The relation of this activation energy to literature values for oxygen diffusion in *Ln*-substituted CeO$_2$ is discussed to infer mechanistic information which can be applied to further develop these materials as solid-state oxide-ion conductors.

Introduction

Solid-state NMR spectra of paramagnetic materials are in general difficult to acquire and interpret due to the large hyperfine interactions between the unpaired electrons and the NMR-active nucleus.[1] Prior paramagnetic solid-state NMR studies have therefore typically focussed on nuclei further removed from the paramagnetic centre, e.g. ^{7}Li in Li-ion battery cathode materials such as transition metal oxides, where the spin-transfer pathways from unpaired electrons to the NMR-active nucleus involve intervening O sites.[2,3] ^{17}O NMR in such systems is hampered not only by the direct bonding interactions between paramagnetic ion and oxygen sites, but also by both the unfavourable natural abundance (0.037%) and quadrupolar character ($I = 5/2$) of the ^{17}O nuclide.[4] Nonetheless, the sensitivity of paramagnetic ^{17}O NMR spectra to distances from, and the electronic and magnetic properties of, the paramagnetic centre has enabled insights in recent years into materials as diverse as metal-organic frameworks,[5] battery materials,[6] mixed ionic-electronic conductors,[7,8] and phases of geological and radiochemical relevance.[9,10] In these studies, computational results from periodic DFT calculations have also played a critical role, aiding in spectral assignment. Nonetheless, the behaviour of paramagnetic

^{17}O NMR shifts even in relatively simple systems, such as polymorphs of the lanthanide oxides and other lanthanide-substituted phases, still remain unexplored.

Lanthanides can have very large electron magnetic moments due to partial filling of the seven *f*-orbitals; moreover, the *f*-orbitals are contracted and hence do not interact strongly with bonded atoms, so that there is minimal crystal field splitting and therefore no driving force to undergo electron pairing and reduce the magnetic moment. These factors result in large paramagnetic NMR shifts, which can complicate spectra and make them challenge to record, but can also provide useful structural information in systems such as lanthanide pyrochlores[11,12] and doped calcium scandate[13], which have applications as catalysts and phosphors. Furthermore, due to the chemical similarity of lanthanides, the lanthanide ion can often be exchanged without significantly changing the structure and bonding of the system, which allows the paramagnetic shifts to be investigated as a function of the electron moment.

The most stable oxidation state for most lanthanides is 3+, corresponding to the sesquioxides Ln_2O_3. The sesquioxides can adopt three different structures: hexagonal (A), monoclinic (B) and cubic (C); with decreasing ionic radius, moving across the lanthanide series, the most stable phase at intermediate temperatures changes from A to B and then to C, although it is sometimes possible to stabilise different polymorphs depending on the thermal history.[14] A survey of the ^{17}O NMR shifts of the lanthanide oxides has previously been made by Yang, Shore and Oldfield,[15] however, their work did not include an example of a sesquioxide with the B-type monoclinic structure (Figure 1a). Of the lanthanides which can adopt the B-type structure, Sm_2O_3 and Eu_2O_3 are the easiest to prepare as the B phases are stable to the lowest temperatures out of the lanthanide sesquioxides (except for Pm_2O_3, but Pm is radioactive); in the present work we have thus chosen these two materials for investigation of their ^{17}O paramagnetic NMR shifts.

The magnetic behaviours of Sm^{3+} and Eu^{3+} are also of interest because both ions have low-lying electronic levels (the first of which are ~1000 cm^{-1} and ~250 cm^{-1} above the ground state for Sm^{3+} and Eu^{3+}, respectively) which have larger magnetic moments than the ground state.[16] This affects the magnetic susceptibility in two ways: firstly, the excited state can be thermally occupied, which increases the effective magnetic moment; secondly, the second-order mixing of these states results in an appreciable temperature-independent Van Vleck susceptibility, particularly for Eu^{3+}. Given that the ground state of Eu^{3+} is non-magnetic to first order ($J = 0$), the effect of the excited state is especially important. The magnetic susceptibility of Sm^{3+} in fact exhibits a broad minimum at around 400 K, due to the competition of the Curie temperature dependence for each level and the Boltzmann population of the excited electronic level with a larger moment. To study the temperature dependence of the Sm^{3+} and Eu^{3+} magnetic susceptibilities, we measure the [17]O paramagnetic shift of cubic Sm_2O_3 and Eu_2O_3 over a wide temperature range. The cubic polymorphs were chosen for this investigation as there is only a single crystallographic oxygen site in this structure,[17] simplifying the spectra.

As was first reported by Lewis et al. for the ^{17}O NMR signal of aqueous solutions of trivalent lanthanide ions,[18] the paramagnetic shift for atoms directly bonded to lanthanides is positive for Ce^{3+}–Sm^{3+} and then negative for Eu^{3+}–Yb^{3+}. The paramagnetic shift in these cases arises from a polarisation mechanism:[18,19] the bonding interaction is primarily between a lone pair on the oxygen and the empty 6s orbital on the lanthanide, which causes a small degree of delocalisation of the electrons onto the lanthanide; then, due to the exchange interaction, the electron density at the lanthanide is polarised parallel to the time-averaged lanthanide electron spin ($\langle S_z \rangle$), leaving a net anti-parallel spin density at the oxygen nucleus, which causes a Fermi-contact shift. The sign and magnitude of this Fermi-contact shift is then determined by the lanthanide electron spin, the variation of which across the lanthanides explains the observed trend in chemical shifts.

The simplest case to consider is Gd^{3+}, which has a spin-only ground term ([8]S): the magnetic moment aligns parallel to the field, which results in an antiparallel spin moment at the oxygen nucleus due to the polarisation mechanism, and hence the negative observed paramagnetic shift. In the second half of

the lanthanide series, Tb^{3+}–Tm^{3+}, the orbital magnetic moment augments the spin magnetic moment (for greater than half-filled shells, spin–orbit coupling favours parallel spin and orbital angular momenta in the ground state), so aligning the magnetic moment parallel to the field still requires a parallel spin moment, resulting in a negative paramagnetic oxygen shift. For Eu^{3+} (with a ^7F ground term), the spin magnetic moment outweighs the orbital magnetic moment, so once again the spin magnetic moment aligns parallel to the field, which yields a negative paramagnetic shift for the oxygen. However, for Ce^{3+}–Sm^{3+}, the orbital magnetic moment is greater than the spin magnetic moment; the orbital magnetic moment therefore aligns parallel to the field and, since for less than half filled shells spin–orbit coupling favours an antiparallel arrangement of the spin and orbital angular momenta in the ground state, this results in an antiparallel spin moment at the lanthanide and therefore a positive paramagnetic shift for oxygen due to the polarisation mechanism. The lanthanide electron spins $\langle S_z \rangle$ have been calculated by Golding and Halton,[19] and Yang et al. showed that there was an excellent correlation between $\langle S_z \rangle$ and the ^{17}O chemical shift in lanthanide oxides.[15]

Among the lanthanide oxides, ceria (CeO_2) is arguably the most technologically important: it finds use as a catalyst in CO oxidation and NO reduction,[20,21] as an oxygen storage material for chemical looping and in automotive catalytic converters,[22,23] and is among the best known isotropic oxide-ion conductors in the intermediate temperature range (400–800 °C).[24–26] This last property is significantly enhanced by means of aliovalent doping, commonly using trivalent lanthanide ions,[26–28] leading to an increase in oxygen vacancy concentration due to charge compensation and a concomitant rise in oxide-ion conductivity. The exemplar phase of this class of conductors is Gd-doped ceria (GDC),[29] which remains a common electrolyte (and anode component) used in solid oxide fuel cells.[30,31] While the conductivity mechanism and activation energy barriers in GDC and other Ln-substituted CeO_2 phases have typically been probed through impedance spectroscopy, DC conductivity, and oxygen permeability methods,[32–37] variable-temperature solid-state NMR studies have also provided complementary and atomic-level insights. Fuda et al. first showed that ^{17}O spin-lattice relaxation (T_1) measurements (up to 1000 °C) of CeO_2 and Y-substituted CeO_2 sensitively probed oxide-ion motion with a component at the Larmor frequency; Adler et al. later reinterpreted the multiple T_1 minima as evidence of two distinct time scales for motion corresponding to nearby oxygen vacancy hops and exchange of the observed oxygen itself with vacancies.[38] Studies by Kim and Stebbins on the Sc-substituted and Y-substituted CeO_2 systems also showed how the ^{17}O (and ^{45}Sc/^{89}Y) chemical shifts reflect the local distribution of aliovalent dopants, with evidence of cation–vacancy pairing.[39,40]

Recent efforts by Heinzmann et al. have shown that ^{17}O NMR (and T_1) measurements can be applied to GDC to quantify doping behaviour and to extract activation energy values that can be ascribed to oxide-ion motion.[41] However, to our knowledge ^{17}O NMR and/or relaxometry-based techniques have not been used to study conduction in other Ln-substituted CeO_2 materials, likely due to the aforementioned difficulties in interpreting NMR spectra of paramagnetic phases. In this work, we apply the lessons learned regarding the magnetic behaviour of Sm^{3+} and Eu^{3+} as seen in the paramagnetic ^{17}O NMR of the monoclinic Ln_2O_3 polymorphs to guide the analysis of variable-temperature ^{17}O spectra of Sm- and Eu-substituted CeO_2.
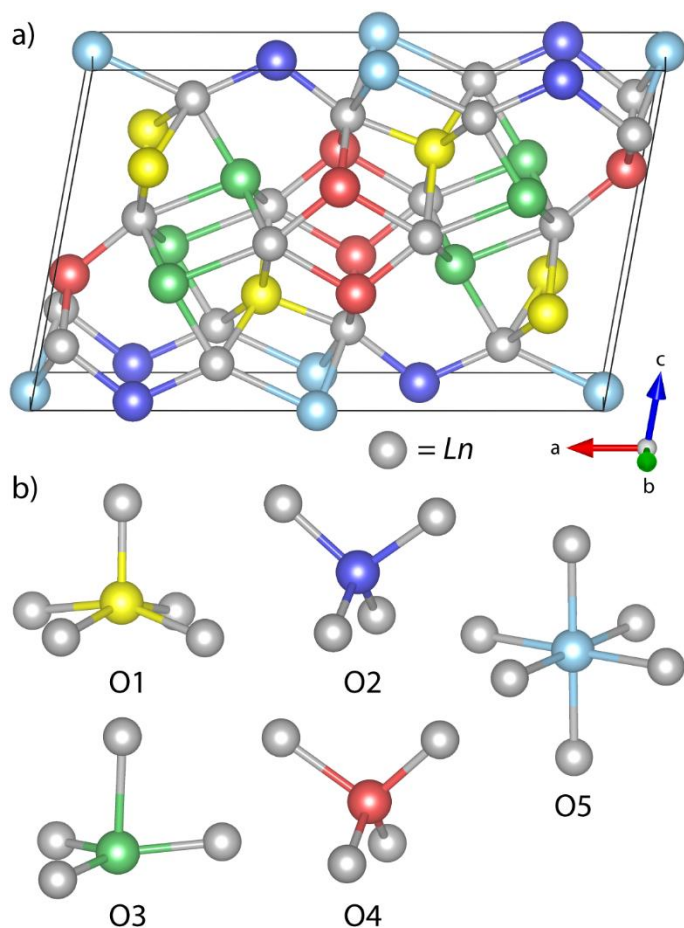
Figure 1: a) Crystal structure, and b) local environments of the crystallographically distinct oxygen sites, of the monoclinic (B) Ln_2O_3 phase. Lanthanide ions are shown in silver and the oxygen ions are coloured according to the different O1 – O5 sites. The structure was generated from ICSD entry 34291 (B-Sm_2O_3),[42] using the VESTA software package[43].

Methods

Synthesis

Cubic Sm_2O_3 was prepared by decomposing $Sm(OH)_3$ (Alfa Aesar, 99%) at 750 °C under air for 12 hours.[44] 15 at% Sm- and Eu-substituted CeO_2 were synthesised by grinding stoichiometric quantities of Sm_2O_3 (Aldrich, 99.9%) or Eu_2O_3 (Acros Organics, 99.99%) and CeO_2 (Aldrich, 99.9%), pelletising at 750 MPa under partial vacuum, and firing at 1500 °C for 48 hours.

[17]O-enriched samples of Sm- and Eu-substituted CeO_2 and cubic Eu_2O_3 were obtained by loading the samples into an alumina tube, which was placed inside a quartz tube filled with [17]O_2 gas (70%, NUKEM Isotopes), sealed with a stopcock, and then annealed at 1000 °C in a tube furnace for 15 hours. Cubic Sm_2O_3 was [17]O-enriched by the same procedure at 750 °C for one week. Monoclinic Sm_2O_3 and Eu_2O_3 were enriched in an alumina tube inside a flame-sealed quartz tube under a [17]O_2 atmosphere, annealed at 1200 °C in a box furnace for 48 hours. Prior to [17]O-enrichment, all Eu_2O_3 samples were dried *in vacuo* at 100 °C and transferred to an argon glovebox for subsequent preparation due to the highly hygroscopic nature of the material.

Characterisation

Powder X-ray diffraction (XRD) patterns were recorded in reflection mode with sample rotation on a PANalytical Empyrean diffractometer emitting Cu Kα (1.540598 Å + 1.544426 Å) radiation. Eu_2O_3 samples were packed into a Kapton sample holder to avoid hydration. Phase identification was achieved by profile matching using the X'Pert HighScore Plus 2.2 software (PANalytical) and by comparison

with the following Inorganic Crystal Structure Database (ICSD) entries: CeO_2 (72155),[45] cubic Sm_2O_3 (40475),[17] monoclinic Sm_2O_3 (34291),[42] cubic Eu_2O_3 (40472)[17] and monoclinic Eu_2O_3 (8056)[46]. Rietveld refinement was performed with the TOPAS academic software package.[47]

NMR

NMR spectra were recorded on a 4.70 T or 7.05 T Bruker Avance III spectrometer or a 7.05 T or 9.40 T Bruker Avance spectrometer, using 1.3, 1.9, 4, or 7 mm probes. Most variable-temperature spectra were acquired by applying heated or cooled nitrogen gas, with cooling achieved either with liquid nitrogen or with a Bruker cooling unit (BCU), except for the high-temperature spectra of cubic Sm_2O_3 and Eu_2O_3 which were acquired by heating the sample with an infrared laser using a 7 mm Bruker laser probe. The sample temperature was determined using an *ex-situ* calibration with the temperature-dependent ^{207}Pb NMR shift of $Pb(NO_3)_2$,[48] except for the laser heated samples where the temperature was determined *in-situ* by grinding the sample with KBr and measuring the temperature-dependent ^{79}Br NMR shift.[49] Spectra were recorded using a Hahn echo with pulse lengths corresponding to optimal excitation in the liquid and quadrupolar limits ($\pi/2$-τ-π-τ-acquire, or $\pi/6$-τ-$\pi/3$-τ-acquire for $I = 5/2$, respectively). The isotropic resonance for the cubic Eu_2O_3 spectra was determined at low temperatures by using a pj-MATPASS sideband separation pulse sequence,[50] and at high temperature by comparison of spectra recorded at 3 and 4 kHz MAS. Longitudinal relaxation constants T_1 were determined by total least-squares refinement of the saturation recovery data to a stretched exponential function using IGOR Pro. Spectra were referenced to liquid H_2O at 0 ppm except for spectra recorded with a 1.9 mm probe which were referenced to CeO_2 at 877 ppm.[51] NMR spectra were processed with Bruker TopSpin 3.5 and deconvoluted using the dmfit software.[52] Full experimental details for each sample are summarised in Table S1, see Supplementary Information.

DFT

Ab initio calculations of the hyperfine coupling constant and electric field gradient parameters for monoclinic Sm_2O_3 and Eu_2O_3 were calculated using the CRYSTAL code.[53] A standard B3LYP functional with 20% or 35% of the Hartree–Fock exchange component (termed 'Hyb20' and 'Hyb35', respectively) was used, as recently demonstrated for ^{17}O shift calculations of paramagnetic systems.[6] Experimental cell structures of Sm_2O_3 and Eu_2O_3 were fully relaxed using the CRYSTAL default criteria with a self-consistent field (SCF) cycle convergence of 10^{-7} Hartree. A Monkhorst-Pack k-mesh of 6×6×6 was used in all cases.

For the lanthanides, we have used a combined core pseudopotential and Gaussian basis set developed by Erba *et al*. which treats the $4f$ levels as valence states.[54] In accordance with the previous study on Ln_2O_3 systems, the oxygen basis set developed by Towler *et al.* was used, with an integration grid consisting of 99 radial points and 1454 angular points.[55] We note that this oxygen basis set was not specifically developed for hyperfine calculations, which need accurate treatment of the core states; more extended oxygen basis sets such as the IGLO-III set were attempted, but resulted in SCF instabilities, presumably arising from the 'mixing' of two basis sets with different qualities.

Results and Discussion

Monoclinic Sm_2O_3 and Eu_2O_3

Monoclinic Sm_2O_3 and Eu_2O_3 were ^{17}O-enriched as detailed in the methodology; the procedure required the use of a flame-sealed quartz tube in a box furnace in order to achieve an enrichment temperature of 1200 ºC, which was necessary to ensure formation of the monoclinic phases.[44] Phase purity was determined by Rietveld refinement of the diffraction pattern (see Supplementary Information §2).

Five crystallographically distinct oxygen sites are present in the monoclinic B-type sesquioxide structure (Figure 1b); however in the room-temperature ^{17}O NMR spectrum of monoclinic Sm_2O_3 (~40 °C sample temperature, Figure 2, top), only four signals can be distinguished. By cooling the sample to −44 °C, the expectation value of the electron spin increases, resulting in larger paramagnetic shifts so that all five resonances can be individually resolved (Figure 2, middle). The observed shift increases with decreasing temperature, indicating that the Curie paramagnetic shift is positive, which is consistent with the paramagnetic shift mechanism as described in the Introduction.

In order to determine the multiplicities of each signal, a quantitative spectrum was recorded with a shorter, quadrupolar $\pi/6$ pulse (Figure 2, bottom), ensuring that quadrupolar nutation effects did not alter the relative signal intensities; the integrated intensities are given in Table 1. The signal at 19 ppm has approximately half the intensity of the other signals, so can be assigned to the O5 (2e) site, which has half the crystallographic multiplicity of the other oxygen sites. The low frequency of this resonance is also consistent with the higher, six-fold (~octahedral) coordination of the O5 site; the paramagnetic contribution to the shift is small for Sm^{3+}, so the chemical shift is dominated by the diamagnetic contribution, and greater coordination typically leads to a lower frequency chemical shift for ^{17}O.[56] Furthermore, by comparing the spectra acquired with different pulse lengths, it can be seen that the sites at 108 ppm and 255 ppm have greater relative intensities in the $\pi/6$ spectrum and thus larger quadrupolar coupling constants, C_Q. In the monoclinic structure (Figure 1), two oxygen sites possess more distorted coordination environments, O1 (4i) which is five-fold coordinated square pyramidal, and O3 (4i) which is four-fold coordinated trigonal pyramidal; these are therefore assigned to the two resonances with larger C_Qs,[57] with the five-fold coordinate O1 having the smaller chemical shift, again due to a lower frequency diamagnetic contribution, consistent with the higher coordination. The remaining two sites, O2 and O4 (4i), have very similar four-fold (~tetrahedral) coordination environments. The shifts of the signals at 162 ppm and 194 ppm are likewise insufficiently different to permit a definitive assignment.

We note that the assigned ^{17}O NMR spectrum of monoclinic Sm_2O_3 is analogous to that of diamagnetic monoclinic Y_2O_3,[58] with the exception that for Y_2O_3 the O3 site resonates at a lower frequency (346 ppm) than O2 and O4 (377 ppm and 383 ppm), and all of the signals are observed in the range 242 – 383 ppm (see Supplementary Information §5), i.e. at significantly more positive frequencies than for Sm_2O_3. Given that for Sm_2O_3 the paramagnetic contribution to the chemical shift is positive, the lower frequency observed shifts for Sm_2O_3 imply a significantly less positive diamagnetic shift contribution, which we attribute to the weak covalency of the Sm–O bonding due to the contracted Sm valence orbitals, since covalent bonding acts to deshield the oxygen and hence increase the chemical shift.[59] The temperature-independent Van Vleck paramagnetism of the ground state, due to mixing in of the low-lying excited state, has a negative contribution to the shift, so will also contribute to the lower frequency shifts observed for Sm_2O_3.[60,61]

Table 1: Summary of the ^{17}O chemical shifts, integrated intensities and assignments for the oxygen sites in monoclinic Sm_2O_3 at −44 °C. The calculated quadrupolar coupling constants C_Q are shown for the Hyb35 functional, see Table S6.

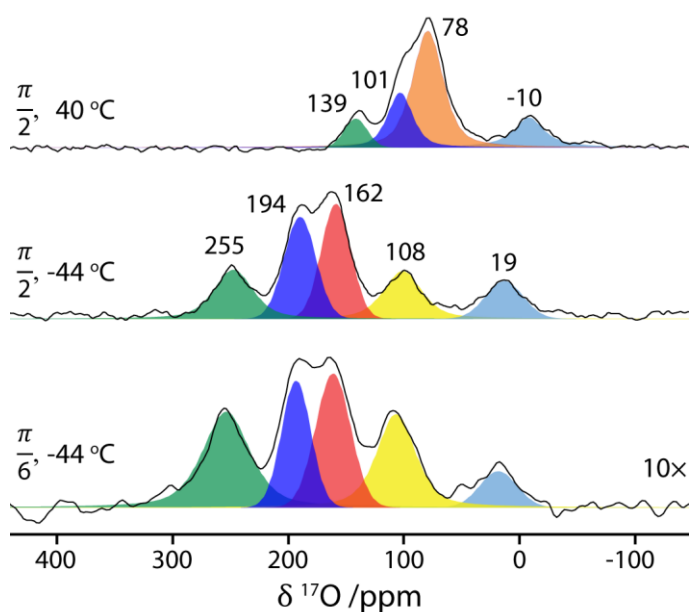| Experimental Shift /ppm	Relative Integration /%	Assignment	Coordination	Calculated C_Q /MHz
19	9	O5 (2e)	~Oct. (6)	0.15
108	24	O1 (4i)	Square pyr. (5)	1.34
162	20	O2, O4 (4i)	~Tet. (4)	0.67
194	20			0.26
255	27	O3 (4i)	Trig. pyr. (4)	1.09

Figure 2: ^{17}O NMR spectra of monoclinic Sm_2O_3 recorded at 9.40 T and 30 kHz MAS with a recycle delay of 0.05 s, with and without sample cooling, and using either Hahn echo pulse sequences with either $\pi/2$ or quadrupolar $\pi/6$ pulses ($\pi/2$-τ-π-τ-acquire or $\pi/6$-τ-$\pi/3$-τ-acquire). The signal observed at 78 ppm in the 40 °C spectrum (orange, top) is attributed to the overlap of the peaks at 162 and 108 ppm observed at −44 °C (red and yellow, respectively).

The ^{17}O NMR spectrum of monoclinic Eu_2O_3 recorded at 4.70 T and 60 kHz MAS is shown in Figure 3, top, with the signals summarised in Table 2; the low field and fast MAS are necessary to sufficiently separate the spinning sidebands due to the wide dispersion of paramagnetic chemical shifts. Four isotropic resonances can be observed, but the signal at −3260 ppm has a significantly higher intensity than the others (which is not due to differential T_1 or T_2 relaxation, although the spectrum is not fully quantitative; see Figure S7), and so is attributed to a superposition of signals from two crystallographic sites. Since the two most similar sites are the O2 and O4 tetrahedrally-coordinated oxygens, this signal is most likely due to these environments; although the O2 and O4 sites could be distinguished in Sm_2O_3, the linewidth for Eu_2O_3 (110 ppm) is significantly larger than for Sm_2O_3 (30 ppm), so it is unsurprising that the signals cannot be resolved for the former. An additional spectrum was recorded at −20 °C, but the two resonances could still not be resolved (Figure S8).

Of the remaining resonances, those at −1850 and −1300 ppm show an increased relative intensity in the $\pi/6$ spectrum so are assigned to the more distorted O1 and O3 sites (comparison of Figure 3, middle and bottom, see Table S2; the higher field of 9.40 T was required to achieve sufficient intensity in the $\pi/6$ spectrum). The diamagnetic shift contribution by which the two sites were distinguished for Sm_2O_3 makes a far smaller relative contribution to the shift in the more paramagnetic Eu_2O_3, so cannot be used to further distinguish the sites; however, on the basis of the larger calculated hyperfine coupling constant A_{iso} (see below), the O3 site is tentatively assigned to the more paramagnetically shifted −1850 ppm signal and O1 therefore to the −1300 ppm signal. By a process of elimination, the signal at −2780 ppm is attributed to the O5 site. To support this assignment, a spectrum with an quantitative recycle delay of 1 s and a $\pi/2$ pulse was recorded (Figure S9); the integrated intensities for each resonance were then weighted by the relative intensities between the spectra recorded with $\pi/2$ and $\pi/6$ pulses to account for the non-quantitative excitation afforded by $\pi/2$ pulses (Table 2, see Table S2 for details). Based on the assignment and crystallographic multiplicities, the relative integrated intensities should occur in the ratio 44:11:22:22, which agrees reasonably well with the experimental values (38:14:24:24), corroborating the assignment.

Table 2: Summary of the ^{17}O chemical shifts, integrated intensities and tentative assignments for the oxygen sites in monoclinic Eu_2O_3 at 45 °C. The calculated hyperfine coupling constants A_{iso} are shown for the Hyb35 functional, see Table S7.

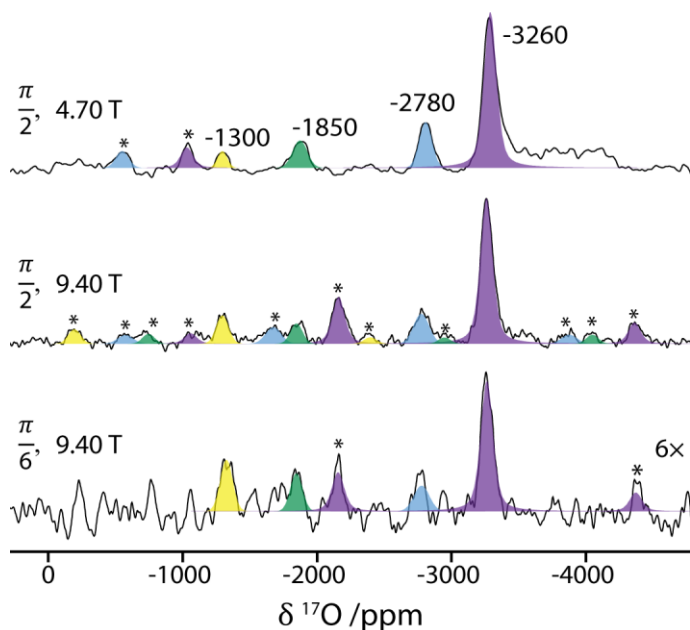| Shift /ppm	Relative Integration /%	Assignment	Coordination	Calculated A_{iso} /MHz
−3260	38	O2, O4 (4i)	~Tet. (4)	−4.02, −3.18
−2780	14	O5 (2e)	~Oct. (6)	−2.04
−1850	24	O3 (4i)	Trig. pyr. (4)	−2.64
−1300	24	O1 (4i)	Square pyr. (5)	−2.04

Figure 3: ^{17}O NMR spectra of monoclinic Eu_2O_3 recorded at 60 kHz MAS and either 4.70 T or 9.40 T, using a Hahn echo with either $\pi/2$ or $\pi/6$ pulses and recycle delays of 0.1 s at 4.70 T and 0.2 s at 9.40 T. Spinning sidebands are marked with an asterisk.

The degree of ^{17}O enrichment for the monoclinic sesquioxides was estimated by comparison with a ^{17}O NMR spectrum of natural abundance H_2O to be ~1% (see Supplementary Information §4). The low enrichment level is most likely to be due to exchange between the $^{17}O_2$ gas and ^{16}O in the quartz tube at the high enrichment temperature (1200 °C); this increases the difficulty of acquiring adequate signal-to-noise, especially for monoclinic Eu_2O_3. Nevertheless, the enrichment level is sufficient to acquire and assign the ^{17}O NMR spectra, as has been shown.

To gain initial quantitative insight into the approximate diamagnetic contributions to the observed shifts, the isotropic ^{17}O chemical shifts for the isostructural diamagnetic analogue Y_2O_3 were calculated using CASTEP[62] (chemical shift calculations in paramagnetic systems are not implemented in CRYSTAL). The calculated chemical shifts for monoclinic Y_2O_3 are in good agreement with the previous experimental results[58] (Table S4), if the experimental assignments of the similar O2 and O4 sites are reversed; furthermore, the calculation confirms the trend of decreasing chemical shift with increasing coordination, which was used to assign the spectrum of Sm_2O_3.

Then, to further explore the spectral assignments for monoclinic Sm_2O_3 and Eu_2O_3, DFT-based calculations of the isotropic hyperfine coupling constant A_{iso} and the quadrupolar coupling constant C_Q were performed in CRYSTAL. Examination of the lattice parameters in the relaxed structures of Sm_2O_3 and Eu_2O_3 (Table S5) shows that the Hyb20 functional (standard B3LYP) significantly overestimates the lattice parameters, whereas the inclusion of 35% HF exchange energy (Hyb35) gives a better agreement to the experimental lattice parameters. As Hyb35 was previously found to yield better agreement with the experimental hyperfine and quadrupolar parameters in our studies of Li-, Na-, and

Mg-transition metal oxides,[63–65] we predict that Hyb35 is also likely to give the more accurate agreement here. Although the use of lower quality oxygen basis sets not specifically designed for hyperfine-type calculations, which is necessary here to be compatible with the available lanthanide basis sets, is likely to hinder the quantitative prediction of these parameters, some qualitative agreements between the experiment and theoretical assignments could be obtained.

As previously noted, the principal contribution to the observed ^{17}O shifts in Sm_2O_3 arises from the chemical shift component, which provides the basis for the assignment. Due to the small paramagnetic contribution, the calculated hyperfine coupling constants A_{iso} cannot be directly correlated to the observed shifts. However, the calculated quadrupolar constants C_Q (Table 1 and Table S6) confirm that the O1 and O3 sites are more distorted, as previously asserted, supporting the assignment of the 108 ppm and 255 ppm signals on the basis of the increased intensity in the $\pi/6$ spectrum. For Eu_2O_3, on the other hand, the paramagnetic shift dominates, so it is informative to inspect the calculated A_{iso} values (Table 2 and Table S7). Despite the imperfect quantitative agreement, qualitative information can still be extracted. The two sites with the largest calculated A_{iso} are O2 and O4, corroborating the assignment of these sites to the most paramagnetically shifted signal at −3260 ppm (although one would expect the signals to have the same A_{iso} given they are observed at the same frequency). The A_{iso} for the other three sites are smaller, and although a less negative experimental shift might therefore be expected for O5, some of this discrepancy may be accounted for by the lower frequency diamagnetic contribution due to the six-fold coordination (as seen for Y_2O_3 and Sm_2O_3). The calculated A_{iso} for O3 is slightly larger than for O1, on which basis the −1300 and −1850 ppm signals are tentatively assigned; although we again stress limitations may arise from the use of a less extensive oxygen basis set, which was not specifically developed to probe the core properties, in order to be compatible with the lanthanide basis sets.

Cubic Sm_2O_3 and Eu_2O_3 – Variable Temperature Spectra

The room temperature ^{17}O NMR spectra of cubic Sm_2O_3 and Eu_2O_3 are shown in Figures S10 and S11, with shifts of 2 ppm and −3075 ppm, respectively. These are in agreement with the previous results of Yang, Shore and Oldfield (10 ppm and −3290 ppm),[15] considering that the additional frictional heating of the faster MAS rate used here will reduce the paramagnetic shift, yielding less positive and less negative shifts for Sm_2O_3 and Eu_2O_3, respectively. The oxygen site in the cubic Ln_2O_3 polymorph is four-fold coordinated, with a geometry intermediate between those of the trigonal pyramidal O3 site and the approximately tetrahedral O2 and O4 sites in the monoclinic structure; this is consistent with the similarity between the cubic Eu_2O_3 ^{17}O shift (−3075 ppm) and the shift of the O2 and O4 sites in monoclinic Eu_2O_3 (−3260 ppm). The ^{17}O shift of cubic Sm_2O_3 (2 ppm), on the other hand, is at a lower frequency than the four-fold coordinated sites in monoclinic Sm_2O_3 (101 ppm and 139 ppm at room temperature); this is most likely to be due to a less positive diamagnetic shift in the cubic phase caused by reduced covalency in the less dense structure (the cell volume per formula unit is 81.6 Å^3 for the cubic structure c.f. 74.8 Å^3 for the monoclinic structure). The enrichment level was estimated for the cubic Sm_2O_3 sample to be 40% (see Supplementary Information §4), which is approaching an ideal enrichment given the 70% enrichment of the $^{17}O_2$ gas; this indicates that at the lower enrichment temperature of 750 °C, there is minimal exchange between the ^{17}O in the gas and the ^{16}O in the quartz tube.

The temperature dependence of the Sm^{3+} and Eu^{3+} magnetism can be explored by measuring the ^{17}O paramagnetic shift over a wide temperature range. Figure 4a shows the ^{17}O shift of cubic Sm_2O_3 as a function of temperature: at lower temperatures the paramagnetic shift increases due to the increased expectation value of the electron spin, as was observed for monoclinic Sm_2O_3 (Figure 2); however, at higher temperatures, there is little temperature dependence of the shift. This behaviour can be most easily seen when plotted as a function of reciprocal temperature (Figure 4b), where a clear deviation

from the linear Curie temperature dependence is seen below around $1000/T = 3 \text{ K}^{-1}$ (T = 333 K). This is due to thermal occupation at the elevated temperatures of an excited state with a higher moment than the ground state.

The ^{17}O shift of Eu_2O_3 exhibits a greater temperature dependence than that of Sm_2O_3 (Figure 4d and e), as expected given the larger paramagnetic shift. The magnetic behaviour of Eu^{3+} is determined by the thermal population of multiple excited levels with different magnetic moments and the Curie temperature dependence of each, combined with a very large Van Vleck paramagnetism of the ground state, which itself has no Curie paramagnetism because $J = 0$. As a result, any agreement between a Curie fit and the experimental data is essentially fortuitous, rather than reflecting any functional dependence. In the case of Sm^{3+}, on the other hand, the ground state has a non-zero moment and there is no appreciable thermal occupation of other levels below ~300 K, so paramagnetic shifts do follow the Curie law below room temperature, as has been shown previously.[61,66]

To quantitatively analyse the temperature dependence of the ^{17}O NMR spectra, the lanthanide electron spins were calculated as a function of temperature using the method of Golding and Halton (see Supplementary Information §6).[19] The linear relationship between the experimental shifts and the calculated electron spins (per unit field) can be seen in Figure 4c and f, and the agreement for Eu_2O_3, in particular, is excellent. From the linear regression, the hyperfine coupling constant (A_{iso}) and diamagnetic shift (δ_0) can be extracted according to

$$\delta_{exp} = \frac{A_{iso}}{\gamma} \times \frac{\langle S_z \rangle}{H} + \delta_0,$$

where γ is the nuclear gyromagnetic ratio; these parameters are shown in Table 3. The hyperfine coupling constants are negative due to the polarisation mechanism mediated by the lanthanide $6s$ orbital (see Introduction), and the value determined for Eu_2O_3 (−2.206 MHz) is in reasonable agreement with that determined by Yang, Shore and Oldfield (−2.7 MHz).[15] The latter was deduced from the relationship between the room temperature ^{17}O shift of different lanthanide sesquioxides and the calculated electron spin, with the assumption that the same hyperfine coupling constant applied across the lanthanide series; A_{iso} will in fact vary across the lanthanide series, and the value obtained by Yang et al. will be skewed towards the values for lanthanides with greater spins, which may partially explain the discrepancy in the values.

Table 3: Hyperfine coupling constants (A_{iso}) and diamagnetic shifts (δ_0) determined assuming a linear regression between the calculated electron spins and the experimental ^{17}O NMR shifts for cubic Sm_2O_3 and Eu_2O_3, as an implicit function of temperature.

	A_{iso} /MHz	δ_0 /ppm
Sm_2O_3	−0.604 ± 0.03	17 ± 2
Eu_2O_3	−2.206 ± 0.005	−44 ± 7

Extrapolating the linear relationship determined for Eu_2O_3 to small electron spins yields shifts which are approximately coincident with the experimental shifts for Sm_2O_3 (Figure 4f), however the linear relationship determined for Sm_2O_3 has a very different gradient to that of Eu_2O_3 (reflected in the different hyperfine coupling constants in Table 5). Given that these materials share the same structure, and that the "average" hyperfine coupling constant across the lanthanide series was determined by Yang, Shore and Oldfield to be −2.7 MHz, it is unlikely that the hyperfine coupling constant for Sm_2O_3 could be as small as −0.604 MHz. Nevertheless, by using the values in Table 5, the calculated shifts match well with the experimental results (Figure 4, solid lines), although the agreement is better for Eu_2O_3.

The discrepancies for Sm_2O_3 may be due to a temperature dependence of the diamagnetic shift being erroneously accounted for in the temperature dependence of the paramagnetic shift, because the paramagnetic shift in Sm_2O_3 is less significant than the diamagnetic shift (as seen for monoclinic Sm_2O_3). Another potential explanation is a pseudo-contact shift, which would have a strong temperature dependence;[1] although normally far less significant than Fermi-contact shifts when the latter is present, a pseudo-contact shift could make a greater contribution in this case because it depends on the anisotropy of the total magnetic moment, rather than the magnitude of the spin which happens to be small for Sm^{3+}. Furthermore, the pseudo-contact shift depends on $1/r^3$ and the internuclear separation, r, is small for direct Ln–O bonding. An estimate of the magnitude of the pseudo-contact shift in cubic Sm_2O_3 is made in §7 of the Supplementary Information, which reveals that it could compete with the diamagnetic and Fermi contact shift contributions.
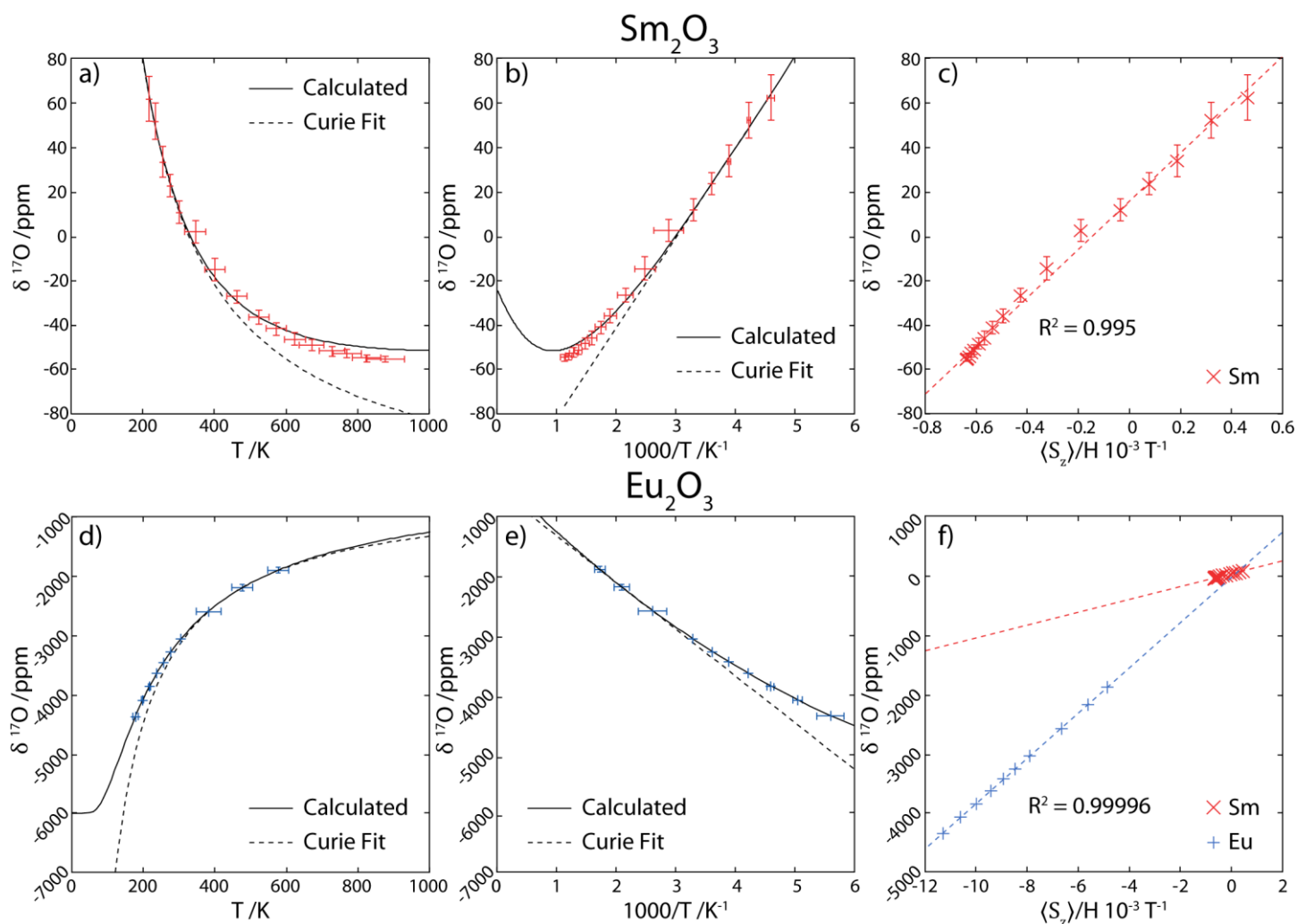

Figure 4: ^{17}O chemical shifts of cubic Sm_2O_3 (a–c) and Eu_2O_3 (d–f) as a function of temperature, reciprocal temperature and calculated electron spin at 9.40 T, recorded with a Hahn echo pulse sequence and recycle delays of 0.05 s and 0.15 s, respectively. The high- and low- temperature spectra were recorded at 4 and 10 kHz MAS, respectively. Shown too are empirical fits assuming a Curie temperature dependence (dashed lines), and the shifts predicted from the calculated electron spin (solid lines). The dashed lines in c) and f) are the linear regressions between the experimental shifts and the calculated electron spins.

Sm- and Eu- Substituted CeO₂

Sm- and Eu-substituted CeO_2 were synthesised as detailed in the methodology. Bulk incorporation of the lanthanide ions was demonstrated by XRD (see Supplementary Information §2), which exclusively showed reflections from the cubic fluorite CeO_2 structure, but with expanded unit cell parameters of

5.433 Å and 5.426 Å respectively, as compared to 5.412 Å for pure CeO$_2$;[45] this is consistent with the ionic radii of the lanthanide ions: Sm^{3+} > Eu^{3+} > Ce^{4+}.[67]

The deconvoluted ^{17}O NMR spectrum of 15 at% Sm-substituted CeO$_2$ (Figure 5a) broadly shows three distinct regions of intensity: ~850 ppm, ~700 ppm and ~550 ppm. A similar spectrum was previously observed for diamagnetic 15 at% Y-substituted CeO$_2$,[39] for which the three regions were ascribed to oxygen environments with zero, one, and two Y nearest neighbours, respectively. Analogously, the signals observed in the three regions here are ascribed to oxygen environments with zero, one, and two Sm nearest neighbours. This assignment is consistent with the lower intensity of the ~550 ppm region, due to the decreased likelihood of having two Sm nearest neighbours (note that the intensity of the ~850 ppm region is not quantitative given the short recycle delay of 1 s).

In addition to the shift caused by Sm nearest neighbours, further splitting of the resonances is observed which, as was also reported for Y-substituted CeO$_2$, is ascribed to nearest neighbour oxygen vacancies; for every two trivalent ions substituted for Ce^{4+}, an oxygen vacancy (v$_O$) is formed. Specifically, the 833 and 694 ppm signals are ascribed to environments with one nearest neighbour oxygen vacancy, and zero or one nearest neighbour Sm atom(s), respectively. The 565 ppm signal (ascribed to two Sm nearest neighbours) is however too broad to distinguish the environments with and without neighbouring oxygen vacancies. Finally, two components can be distinguished for the highest frequency signal with no Sm or oxygen vacancy nearest neighbours: a sharper component centred at 877 ppm and a broad component at 879 ppm. The former is assigned to environments with the pure CeO$_2$ structure and no substitution in the long-range vicinity, consistent with the very sharp peak of pure CeO$_2$ at 877 ppm,[51] while the latter is ascribed to environments with next-nearest neighbour Sm substitution and/or oxygen vacancies resulting in a heterogeneously broadened signal.

These assignments could be corroborated by recording a second spectrum at lower temperature (Table 4 and Figure S12). The paramagnetic shift due to Sm is small and positive (as observed for Sm$_2$O$_3$), the magnitude of which increases at lower temperatures; consequently, the observed chemical shift also increases (becomes more positive) at lower temperature for the signals with Sm nearest neighbours, with the greatest increase seen for the environment with two Sm nearest neighbours. Although the paramagnetic shift is positive, the net effect of Sm nearest neighbours is to reduce the ^{17}O shift, because the diamagnetic shift contribution dominates. Furthermore, the change in diamagnetic shift is greater (more negative) for Sm substitution (~150 ppm/Sm) than for Y substitution (~50 ppm/Y), which is consistent with the less positive diamagnetic chemical shifts observed for Sm$_2$O$_3$ than for Y$_2$O$_3$ (see above).

Table 4: Summary of ^{17}O environments in Sm-substituted CeO$_2$, with the number of Sm and oxygen vacancy (v$_O$) nearest neighbours, and the chemical shifts observed at 56 °C and −12 °C.

Assignment	Shift @ 56 °C /ppm	Shift @ −12 °C /ppm	Difference /ppm
0×Sm, 0×v$_O$	877	876	−1
	879		−3
0×Sm, 1×v$_O$	833	829	−4
1×Sm, 0×v$_O$	737	740	+3
1×Sm, 1×v$_O$	694	700	+5
2×Sm	565	576	+11

In order to investigate oxygen diffusion in Sm-substituted CeO$_2$, the spin-lattice relaxation (T_1) constants for each site were measured as a function of temperature (Figure 5b); the T_1 of the sharp component at 877 ppm was too long to practically measure in a reasonable time frame. The environments with Sm nearest neighbours have markedly short T_1 constants (on the order of 1 – 10 ms) due to paramagnetic relaxation enhancement,[1] for which there is no appreciable temperature dependence. The T_1 constants for the 879 ppm and 833 ppm signals, on the other hand, exhibit a clear

Arrhenius temperature dependence with a positive gradient, which is evidence of motion faster than the Larmor frequency (27 MHz at 4.70 T).[38,68] At the lowest temperature, the T_1 constants deviate from Arrhenius behaviour, which is ascribed to the contribution of a different relaxation mechanism that begins to outweigh the relaxation due to motion. The gradients are equivalent within error for both resonances and correspond to an activation energy of (0.35 ± 0.01) eV. The lack of Arrhenius dependence for the T_1 constants of the environments with Sm nearest neighbours is attributable to the rapid paramagnetic relaxation, which dominates over the relaxation induced by oxygen motion.
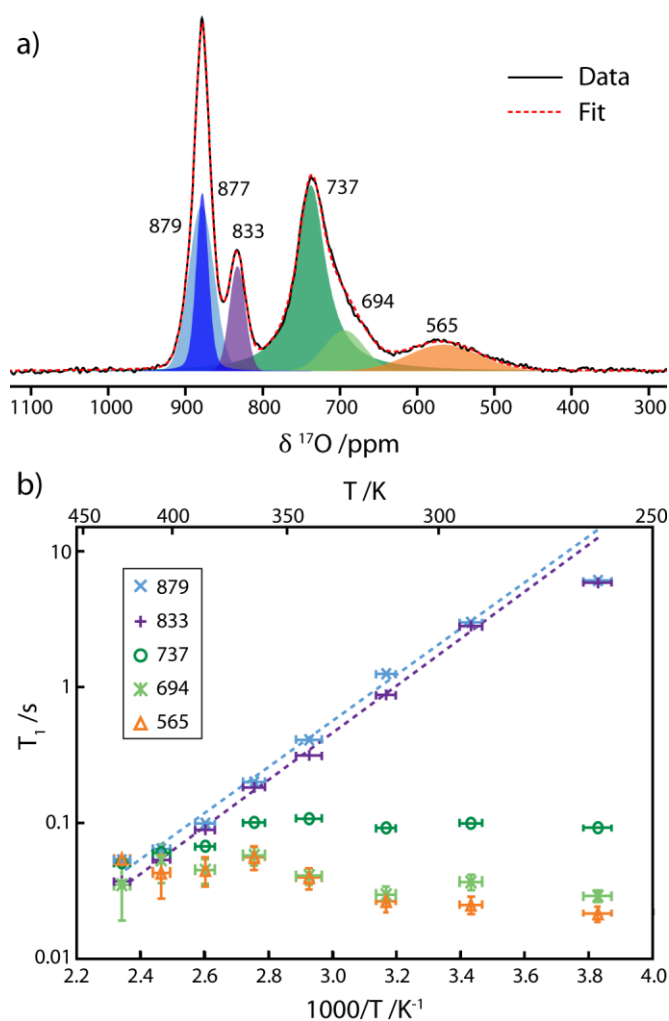

Figure 5: a) Deconvoluted ^{17}O NMR spectrum of 15 at% Sm-substituted CeO_2, recorded at 7.05 T and 40 kHz MAS, with a Hahn echo pulse sequence and a recycle delay of 1 s. b) Arrhenius plot of the T_1 for each environment as a function of temperature, measured with a saturation recovery experiment at 4.70 T and 14 kHz MAS.

The ^{17}O NMR spectrum of Eu-substituted CeO_2 (Figure 6a) is similar to that of Sm-substituted CeO_2, but spans a much wider range, because the paramagnetic shift due to Eu is both larger than that for Sm, and negative so that it reinforces the change in diamagnetic shift. The signal for environments with no Eu nearest neighbours, centred at 867 ppm, is broader than that for Sm-substituted CeO_2 due to interactions with next-nearest-neighbour Eu ions and the pseudo-contact shift[1]; however, a shoulder can be distinguished, centred at 839 ppm, which is ascribed to environments with a nearest-neighbour oxygen vacancy. A second signal can also be observed at 267 ppm, which is ascribed to environments with a nearest-neighbour Eu atom. In order to identify further signals which arise from environments with Eu nearest neighbours, a T_1-filtered spectrum was acquired (Figure 6b), by taking the difference between spectra recorded with recycle delays of 1 s and 0.1 s, scaled so as to remove the slower-relaxing

signal at ~850 ppm; this highlights additional intensity between 0 and −1000 ppm. As the chemical shift contribution from lanthanide neighbours is approximately additive,[11] the signal at −498 ppm is ascribed to environments with two Eu nearest neighbours.

There are two further resonances which can be distinguished, at −106 ppm and −911 ppm. These are similar to the shoulders observed for Sm- and Y-substituted CeO_2, which were assigned to nearest-neighbour oxygen vacancies; however for Eu-CeO_2 the additional signals are shifted to lower frequency by ~400 ppm relative to the main resonance, compared to 44 ppm and 20 ppm for Sm- and Y-CeO_2 respectively. These signals in Eu-CeO_2 are therefore instead assigned to environments with one and two nearest-neighbour Eu ions respectively, where (one of) the adjacent Eu atom(s) has an oxygen vacancy in *its* nearest-neighbour coordination shell: this undercoordination of the Eu atom will result in stronger bonding to the oxygen of interest, and hence a larger transferred spin density and a greater paramagnetic shift. This is consistent with the greater relative intensity of the −911 ppm signal to the −498 ppm signal, compared with that of the −106 ppm signal to the 267 ppm signal, because the former signals arise from environments with two Eu nearest-neighbours, and so are more likely to have an oxygen vacancy in the coordination shell of one of the ions.

To confirm the assignment, a second spectrum was recorded at a lower temperature (Table 5, Figure S13). The shift for environments with nearest-neighbour Eu atoms decreases at lower temperature, due to an increase in the expectation value of the electron spin and hence in the magnitude of the paramagnetic shift. Furthermore, the amount by which the paramagnetic shift increases (becomes more negative) scales with the magnitude of the paramagnetic shift, i.e. the more shifted signals decrease in frequency even further. This corroborates the increased hyperfine coupling due to a second Eu nearest-neighbour or due to the presence of an oxygen vacancy in the coordination shell of a nearest-neighbour Eu atom.

Table 5: Summary of the ^{17}O environments in Eu-substituted CeO_2, and the chemical shifts observed at 46 °C and 8 °C..

Assignment	Shift @ 46 °C /ppm	Shift @ 8 °C /ppm	Difference /ppm
0×Eu, 0×v_O	867	867	0
0×Eu, 1×v_O	839	836	−3
1×Eu	267	215	−52
1×Eu + v_O	−106	−175	−69
2×Eu	−498	−571	−73
2×Eu + v_O	−911	−1014	−103

To investigate oxygen diffusion in Eu-substituted CeO_2, the T_1 constants were similarly measured as a function of temperature (Figure 6c). The lower temperature experiments were performed at 40 kHz MAS, which allowed the 267 ppm resonance to be distinguished, however the T_1 constants for the lower frequency signals could not be measured accurately due to insufficient signal-to-noise levels. The higher temperature experiments were performed at 14 kHz MAS, which was insufficient to resolve the 267 ppm signal. A similar result is observed as for the Sm-substituted CeO_2: the lower frequency signal at 267 ppm, ascribed to environments with a Eu nearest neighbour, possesses a short T_1 constant (~1 s) induced by paramagnetic relaxation, which shows no significant temperature dependence over the observable range. The higher-frequency ~865 ppm signal, on the other hand, again displays a marked Arrhenius-like temperature dependence of its T_1 constant, which corresponds to an activation energy of (0.34 ± 0.02) eV for both components.
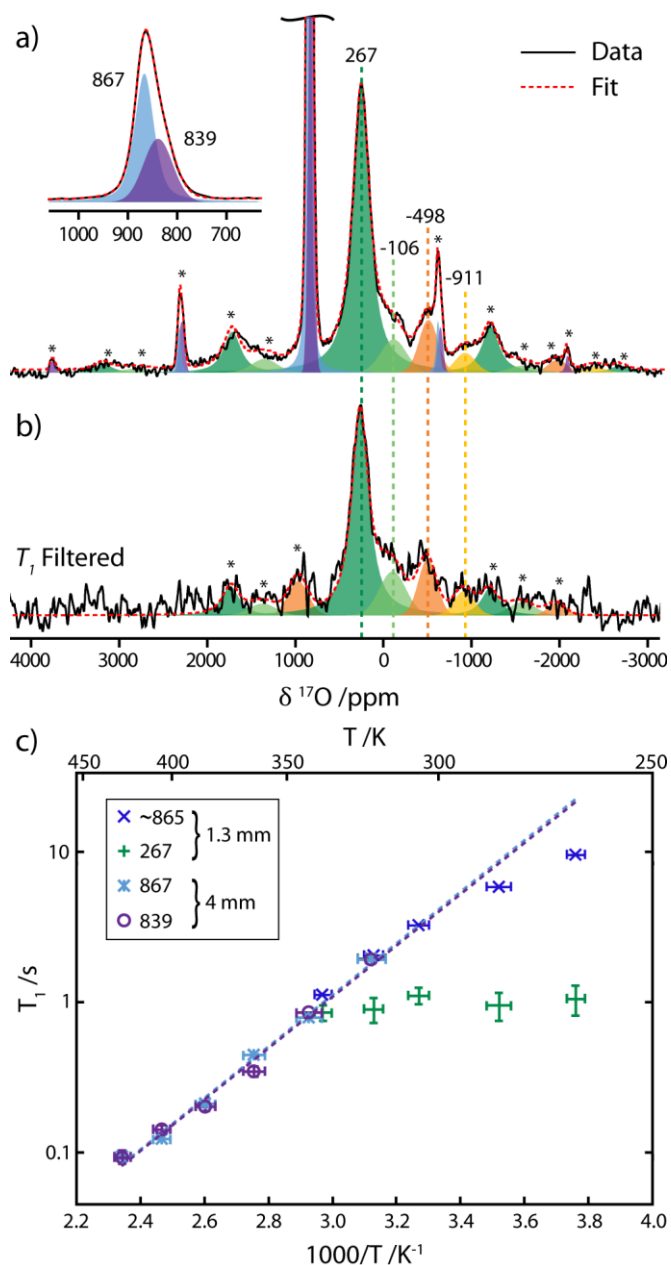
Figure 6: a) Deconvoluted ^{17}O NMR spectrum of 15 at% Eu-substituted CeO_2, recorded at 7.05 T and 60 kHz MAS, with a Hahn echo pulse sequence and a recycle delay of 1 s, as well as an expansion of the ~865 ppm signal. b) T_1-filtered ^{17}O spectrum, obtained by taking the difference between two spectra recorded with recycle delays of 1 s and 0.1 s, scaled so as to remove the ~865 ppm signal with a longer T_1 constant. Sidebands are marked with an asterisk. c) Arrhenius plot of the T_1 constants as a function of temperature at 7.05 T. The lower temperature experiments were performed with a 1.3 mm probe at 40 kHz MAS; the two components of the ~865 ppm signal were not sufficiently distinct to be differentiated. The higher temperature experiments were performed with a 4 mm probe at 14 kHz MAS, for which both components of the ~865 ppm signal could be distinguished, but the 267 ppm resonance could not be resolved.

Oxygen diffusion in CeO_2 is known to arise from the motion of oxygen vacancies,[25,26] which in this case are introduced by substitution with trivalent ions. The motion of these vacancies causes fluctuations in the electric field gradient at an oxygen nucleus and hence in the quadrupolar coupling, thereby inducing longitudinal relaxation.[38,69] The activation energies for oxygen vacancy motion in Sm- and Eu-substituted CeO_2 determined here are the same within error; this supports the prevalent assumption that the activation energy for vacancy hops is largely independent of the substituent.[25]

The activation energy for oxygen diffusion in 15 at% Sm-substituted CeO_2 has previously been reported as 1.00 eV from the DC conductivity[34] and 0.84 eV from impedance spectroscopy[35]. An activation energy for oxygen diffusion in 15 at% Eu-substituted CeO_2 has not been reported to our knowledge, but impedance spectroscopy experiments have yielded activation energies for 10 at% and 20 at% Eu-substituted CeO_2 of 0.64 eV and 0.89 eV, respectively.[36,37]

These values are all significantly higher than the activation energies observed here (0.35 eV). The discrepancy between the activation energies determined by NMR and by other techniques for oxygen diffusion has been discussed by Kim et al.,[70] and was ascribed to two main factors. Firstly, bulk diffusion techniques measure the motion of vacancies that contributes to the macroscopic transport, whereas NMR is sensitive to any vacancy motion; in particular if a vacancy hops back after a forward hop it will contribute to nuclear relaxation but not to bulk diffusion. Secondly, vacancies can be trapped by defects: at low temperatures the positively charged oxygen vacancies associate with the negatively charged trivalent ion substitutional defects.[25] The activation energy for bulk diffusion includes the energy required to dissociate these vacancy–defect pairs, whereas nuclear relaxation can be caused by vacancy hops where the vacancy remains associated. An association energy of ~0.5 eV can be predicted for trivalent substituents on the basis of a point-defect model,[71] which brings the activation energy observed here more in line with the values for bulk oxygen transport.

The point-defect model is insufficient, however, to explain the variations in the total activation energy for oxygen motion with different trivalent substituents, as in this case the charge on the defects is the same; instead one must also consider the degree of lattice strain, which also acts to trap oxygen vacancies, so that the lowest association energy is observed when the ionic radius of the substituent matches that of Ce^{4+}.[25] The ionic radius of Eu^{3+} (1.09 Å) is closer to that of Ce^{4+} (1.01 Å) than to that of Sm^{3+} (1.10 Å),[67] which explains the lower activation energies for overall vacancy diffusion reported in the literature for Eu-CeO_2, as the association energy will be lower than for Sm-CeO_2; however, as our results show, the activation energies for vacancy *motion* are the same, in agreement with the current understanding of ionic transport in CeO_2.

Conclusions

The ^{17}O NMR spectra for monoclinic Sm_2O_3 and Eu_2O_3 have been reported for the first time and the resonances assigned, primarily on the basis of the integrated intensities and the magnitude of the quadrupolar coupling constants. Further assignment for Sm_2O_3 is based on the diamagnetic chemical shifts as estimated from the O coordination, which dominate for Sm_2O_3 due to the modest magnetic susceptibility of Sm^{3+} and hence small paramagnetic shifts. DFT calculations of the quadrupolar and hyperfine coupling constants provide qualitative insights and help to corroborate the assignments, as well as permit a tentative assignment of two otherwise unassignable resonances in Eu_2O_3.

The effect of low-lying excited electronic states on the magnetic susceptibilities of Sm^{3+} and Eu^{3+} have been investigated by recording the ^{17}O spectra of the cubic sesquioxides over a wide temperature range. In particular, above room temperature the shift of Sm_2O_3 deviates from Curie temperature dependence due to the thermal population of an excited state with a greater magnetic moment, while the shift of Eu_2O_3 at lower temperatures is dominated by the temperature-independent Van Vleck paramagnetism of the ground state. The electron spin ($\langle S_z \rangle$) was calculated as a function of temperature, yielding predicted shifts which reproduce the aforementioned behaviour and agree well with experiment.

The ^{17}O NMR spectra have also been recorded for 15 at% Sm- and Eu- substituted CeO_2 which reveal signals due to environments with zero, one and two *Ln* nearest neighbours, as well as further splitting due to the presence of oxygen vacancies. The T_1 constants have been measured as a function of temperature and while the environments with *Ln* nearest neighbours show largely temperature-independent short T_1 constants due to the paramagnetic relaxation enhancement, the T_1 constants for environments without *Ln* nearest neighbours exhibit a clear Arrhenius temperature dependence,

corresponding to an activation energy of 0.35 eV, which is the same within error for both Sm- and Eu- substituted CeO_2 and for environments both with and without nearest neighbour oxygen vacancies. This Arrhenius behaviour is ascribed to motion of oxygen vacancies and the activation energy is compared to literature values for oxygen transport: NMR is sensitive to local motion, so does not include the vacancy–defect association energy which also contributes to the activation energy for bulk oxygen motion, explaining the larger activation energies reported in these materials using other techniques.

The paramagnetic NMR study presented here highlights the adversities that are commonly faced in such systems due to poor signal-to-noise levels as well as broad dispersions of hyperfine shifts, but also reveals the structural and mechanistic insights that can be attained, whilst providing examples of strategies to overcome these difficulties. Furthermore, the challenges and successes in using DFT methods to predict NMR parameters in paramagnetic lanthanide oxides are demonstrated for the first time. The understanding gained by a combination of these experimental and theoretical methods allows us to explore the local oxygen environments and vacancy motion in *Ln*-substituted CeO_2, which may aid in future improvements of their performance as solid-state oxide-ion conductors. We also hope that the specific techniques described in the present study will enable detailed paramagnetic ^{17}O NMR studies of other as-yet unexplored systems by adventurous spectroscopists.

References

(1)   Pell, A. J.; Pintacuda, G.; Grey, C. P. Paramagnetic NMR in Solution and the Solid State. *Prog. Nucl. Magn. Reson. Spectrosc.* **2019**, *111*, 1–271.

(2)   Ménétrier, M.; Saadoune, I.; Levasseur, S.; Delmas, C. The Insulator-Metal Transition upon Lithium Deintercalation from $LiCoO_2$: Electronic Properties and ^{7}Li NMR Study. *J. Mater. Chem.* **1999**, *9* (5), 1135–1140.

(3)   Grey, C. P.; Dupré, N. NMR Studies of Cathode Materials for Lithium-Ion Rechargeable Batteries. *Chem. Rev.* **2004**, *104* (10), 4493–4512.

(4)   Gerothanassis, I. P. Oxygen-17 NMR Spectroscopy: Basic Principles and Applications (Part I). *Prog. Nucl. Magn. Reson. Spectrosc.* **2010**, *56* (2), 95–197.

(5)   Kong, X.; Terskikh, V. V; Khade, R. L.; Yang, L.; Rorick, A.; Zhang, Y.; He, P.; Huang, Y.; Wu, G. Solid-State ^{17}O NMR Spectroscopy of Paramagnetic Coordination Compounds. *Angew. Chemie Int. Ed.* **2015**, *54* (16), 4753–4757.

(6)   Seymour, I. D.; Middlemiss, D. S.; Halat, D. M.; Trease, N. M.; Pell, A. J.; Grey, C. P. Characterizing Oxygen Local Environments in Paramagnetic Battery Materials via ^{17}O NMR and DFT Calculations. *J. Am. Chem. Soc.* **2016**, *138* (30), 9405–9408.

(7)   Halat, D. M.; Dervişoğlu, R.; Kim, G.; Dunstan, M. T.; Blanc, F.; Middlemiss, D. S.; Grey, C. P. Probing Oxide-Ion Mobility in the Mixed Ionic–Electronic Conductor $La_2NiO_{4+\delta}$ by Solid-State ^{17}O MAS NMR Spectroscopy. *J. Am. Chem. Soc.* **2016**, *138* (36), 11958–11969.

(8)   Halat, D. M.; Dunstan, M. T.; Gaultois, M. W.; Britto, S.; Grey, C. P. Study of Defect Chemistry in the System $La_{2-x}Sr_xNiO_{4+\delta}$ by ^{17}O Solid-State NMR Spectroscopy and Ni K-Edge XANES. *Chem. Mater.* **2018**, *30* (14), 4556–4570.

(9)   McCarty, R. J.; Stebbins, J. F. Transition Metal Dopant Cation Distributions in MgO and CaO: New Inferences from Paramagnetically Shifted Resonances in ^{17}O, ^{25}Mg, and ^{43}Ca NMR Spectra. *J. Phys. Chem. C* **2016**, *120* (20), 11111–11120.

(10)   Martel, L.; Magnani, N.; Vigier, J.-F.; Boshoven, J.; Selfslag, C.; Farnan, I.; Griveau, J.-C.; Somers, J.; Fanghänel, T. High-Resolution Solid-State Oxygen-17 NMR of Actinide-Bearing Compounds: An Insight into the 5f Chemistry. *Inorg. Chem.* **2014**, *53* (13), 6928–6933.

(11)   Cheetham, A. K.; Dobson, C. M.; Grey, C. P.; Jakeman, R. J. B. Paramagnetic Shift Probes in High-Resolution Solid-State NMR. *Nature* **1987**, *328* (6132), 706–707.

(12)   Grey, C. P.; Smith, M. E.; Cheetham, A. K.; Dobson, C. M.; Dupree, R. Yttrium-89 Magic Angle Spinning NMR Study of Rare-Earth Pyrochlores: Paramagnetic Shifts in the Solid State. *J. Am. Chem. Soc.* **1990**, *112* (12), 4670–4675.

(13)   George, N. C.; Brgoch, J.; Pell, A. J.; Cozzan, C.; Jaffe, A.; Dantelle, G.; Llobet, A.; Pintacuda, G.; Seshadri, R.; Chmelka, B. F. Correlating Local Compositions and Structures with the Macroscopic Optical Properties of Ce^{3+}-Doped $CaSc_2O_4$, an Efficient Green-Emitting Phosphor. *Chem. Mater.* **2017**, *29* (8), 3538–3546.

(14)   Adachi, G.; Imanaka, N. The Binary Rare Earth Oxides. *Chem. Rev.* **1998**, *98* (4), 1479–1514.

(15)   Yang, S.; Shore, J.; Oldfield, E. Oxygen-17 Nuclear Magnetic Resonance Spectroscopic Study of the Lanthanide Oxides. *J. Magn. Reson.* **1992**, *99* (2), 408–412.

(16)   Van Vleck, J. H. *Handbook of Optics: The Theory of Electric and Magnetic Susceptibilities*; Oxford Univ. Press: Oxford, 1965.

(17)   Saiki, A.; Ishizawa, N.; Mizutani, N.; Kato, M. Structural Change of C-Rare Earth Sesquioxides Yb_2O_3 and Er_2O_3 as a Function of Temperature. *Yogyo Kyokai-Shi* **1985**, *93* (10), 649–654.

(18)   Lewis, W. B.; Jackson, J. A.; Lemons, J. F.; Taube, H. Oxygen-17 NMR Shifts in Aqueous Solutions of Rare-Earth Ions. *J. Chem. Phys.* **1962**, *36* (3), 694–701.

(19)   Golding, R.; Halton, M. A Theoretical Study of the ^{14}N and ^{17}O N.M.R. Shifts in Lanthanide Complexes. *Aust. J. Chem.* **1972**, *25* (12), 2577.

(20)   Carrettin, S.; Concepción, P.; Corma, A.; López Nieto, J. M.; Puntes, V. F. Nanocrystalline CeO_2 Increases the Activity of Au for CO Oxidation by Two Orders of Magnitude. *Angew. Chemie Int. Ed.* **2004**, *43* (19), 2538–2540.

(21)   Qi, G.; Yang, R. T.; Chang, R. MnO_x-CeO_2 Mixed Oxides Prepared by Co-Precipitation for Selective Catalytic Reduction of NO with NH_3 at Low Temperatures. *Appl. Catal. B Environ.* **2004**, *51* (2), 93–106.

(22)   Galvita, V. V.; Poelman, H.; Bliznuk, V.; Detavernier, C.; Marin, G. B. CeO_2-Modified Fe_2O_3 for CO_2 Utilization via Chemical Looping. *Ind. Eng. Chem. Res.* **2013**, *52* (25), 8416–8426.

(23)   Trovarelli, A. Catalytic Properties of Ceria and CeO_2-Containing Materials. *Catal. Rev.* **1996**, *38* (4), 439–520.

(24)   Kevane, C. J.; Holverson, E. L.; Watson, R. D. Electrolytic Conduction in Calcium-Doped Solid Cerium Oxide. *J. Appl. Phys.* **1963**, *34* (7), 2083–2087.

(25)   Inaba, H.; Tagawa, I. Ceria-Based Solid Electrolytes. *Solid State Ionics* **1996**, *83* (1–2), 1–16.

(26)   Etsell, T. H.; Flengas, S. N. Electrical Properties of Solid Oxide Electrolytes. *Chem. Rev.* **1970**,

70 (3), 339–376.

(27)   Kudo, T. Oxygen Ion Conduction of the Fluorite-Type $Ce_{1-x}Ln_xO_{2-x/2}$ (Ln = Lanthanoid Element). *J. Electrochem. Soc.* **1975**, *122* (1), 142–147.

(28)   Tuller, H. L. Doped Ceria as a Solid Oxide Electrolyte. *J. Electrochem. Soc.* **1975**, *122* (2), 255.

(29)   Kudo, T. Mixed Electrical Conduction in the Fluorite-Type $Ce_{1-x}Gd_xO_{2-x/2}$. *J. Electrochem. Soc.* **1976**, *123* (3), 415.

(30)   Baertsch, C. D.; Jensen, K. F.; Hertz, J. L.; Tuller, H. L.; Vengallatore, S. T.; Spearing, S. M.; Schmidt, M. A. Fabrication and Structural Characterization of Self-Supporting Electrolyte Membranes for a Micro Solid-Oxide Fuel Cell. *J. Mater. Res.* **2004**, *19* (09), 2604–2615.

(31)   Ishihara, T. Nickel–Gd-Doped CeO_2 Cermet Anode for Intermediate Temperature Operating Solid Oxide Fuel Cells Using $LaGaO_3$-Based Perovskite Electrolyte. *Solid State Ionics* **2000**, *132* (3–4), 209–216.

(32)   Lai, W.; Haile, S. M. Impedance Spectroscopy as a Tool for Chemical and Electrochemical Analysis of Mixed Conductors: A Case Study of Ceria. *J. Am. Ceram. Soc.* **2005**, *88* (11), 2979–2997.

(33)   Kharton, V. V.; Kovalevsky, A. V.; Viskup, A. P.; Figueiredo, F. M.; Yaremchenko, A. A.; Naumovich, E. N.; Marques, F. M. B. Oxygen Permeability of $Ce_{0.8}Gd_{0.2}O_{2-\delta}$–$La_{0.7}Sr_{0.3}MnO_{3-\delta}$ Composite Membranes. *J. Electrochem. Soc.* **2000**, *147* (7), 2814–2821.

(34)   Fu, Y. P.; Wen, S. B.; Lu, C. H. Preparation and Characterization of Samaria-Doped Ceria Electrolyte Materials for Solid Oxide Fuel Cells. *J. Am. Ceram. Soc.* **2008**, *91* (1), 127–131.

(35)   Wattanathana, W.; Veranitisagul, C.; Wannapaiboon, S.; Klysubun, W.; Koonsaeng, N.; Laobuthee, A. Samarium Doped Ceria (SDC) Synthesized by a Metal Triethanolamine Complex Decomposition Method: Characterization and an Ionic Conductivity Study. *Ceram. Int.* **2017**, *43* (13), 9823–9830.

(36)   Cioateră, N.; Pârvulescu, V.; Rolle, A.; Vannier, R. N. Effect of Strontium Addition on Europium-Doped Ceria Properties. *Solid State Ionics* **2009**, *180* (9–10), 681–687.

(37)   Balazs, G. B.; Glass, R. S. Ac Impedance Studies of Rare Earth Oxide Doped Ceria. *Solid State Ionics* **1995**, *76* (1–2), 155–162.

(38)   Adler, S. B.; Smith, J. W.; Reimer, J. A. Dynamic Monte Carlo Simulation of Spin-Lattice Relaxation of Quadrupolar Nuclei in Solids. Oxygen-17 in Yttria-Doped Ceria. *J. Chem. Phys.* **1993**, *98* (9), 7613–7620.

(39)   Kim, N.; Stebbins, J. F. Vacancy and Cation Distribution in Yttria-Doped Ceria: An [89]Y and ^{17}O MAS NMR Study. *Chem. Mater.* **2007**, *19* (23), 5742–5747.

(40)   Kim, N.; Hsieh, C. H.; Stebbins, J. F. Scandium Coordination in Solid Oxides and Stabilized Zirconia: [45]Sc NMR. *Chem. Mater.* **2006**, *18* (16), 3855–3859.

(41)   Heinzmann, R.; Issac, I.; Eufinger, J.-P.; Ulbrich, G.; Lerch, M.; Janek, J.; Indris, S. Observing Local Oxygen Interstitial Diffusion in Donor-Doped Ceria by ^{17}O NMR Relaxometry. *J. Phys. Chem. C* **2016**, *120* (16), 8568–8577.

(42)   Cromer, D. T. The Crystal Structure of Monoclinic Sm_2O_3. *J. Phys. Chem.* **1957**, *61* (6), 753–755.

(43)   Momma, K.; Izumi, F. VESTA 3 for Three-Dimensional Visualization of Crystal, Volumetric and Morphology Data. *J. Appl. Crystallogr.* **2011**, *44* (6), 1272–1276.

(44)   Meyer, G.; Morss, L. R. Synthesis of Lanthanide and Actinide Compounds. In *Topics in f-*

Element Chemistry; Sinha, S. P., Ed.; Springer Science & Business Media: Dordrecht, 2012; Vol. 2.

(45)   WoŁcyrz, M.; Kepinski, L. Rietveld Refinement of the Structure of CeOCl Formed in Pd/CeO$_2$ Catalyst: Notes on the Existence of a Stabilized Tetragonal Phase of La$_2$O$_3$ in LaPdO System. *J. Solid State Chem.* **1992**, *99* (2), 409–413.

(46)   Yakel, H. L. A Refinement of the Crystal Structure of Monoclinic Europium Sesquioxide. *Acta Crystallogr. Sect. B* **1979**, *35* (3), 564–569.

(47)   Coelho, A. A. Indexing of Powder Diffraction Patterns by Iterative Use of Singular Value Decomposition. *J. Appl. Crystallogr.* **2003**, *36* (1), 86–95.

(48)   Bielecki, A.; Burum, D. P. Temperature Dependence of ^{207}Pb MAS Spectra of Solid Lead Nitrate. An Accurate, Sensitive Thermometer for Variable-Temperature MAS. *J. Magn. Reson. Ser. A* **1995**, *116*, 215–220.

(49)   Thurber, K. R.; Tycko, R. Measurement of Sample Temperatures under Magic-Angle Spinning from the Chemical Shift and Spin-Lattice Relaxation Rate of ^{79}Br in KBr Powder. *J. Magn. Reson.* **2009**, *196* (1), 84–87.

(50)   Hung, I.; Zhou, L.; Pourpoint, F.; Grey, C. P.; Gan, Z. Isotropic High Field NMR Spectra of Li-Ion Battery Materials with Anisotropy >1 MHz. *J. Am. Chem. Soc.* **2012**, *134* (4), 1898–1901.

(51)   Oldfield, E.; Coretsopoulos, C.; Yang, S.; Reven, L.; Lee, H. C.; Shore, J.; Han, O. H.; Ramli, E.; Hinks, D. ^{17}O Nuclear-Magnetic-Resonance Spectroscopic Study of High-Tc Superconductors. *Phys. Rev. B* **1989**, *40* (10), 6832–6849.

(52)   Massiot, D.; Fayon, F.; Capron, M.; King, I.; Le Calvé, S.; Alonso, B.; Durand, J.-O.; Bujoli, B.; Gan, Z.; Hoatson, G. Modelling One- and Two-Dimensional Solid-State NMR Spectra. *Magn. Reson. Chem.* **2002**, *40* (1), 70–76.

(53)   Dovesi, R.; Erba, A.; Orlando, R.; Zicovich-Wilson, C. M.; Civalleri, B.; Maschio, L.; Rérat, M.; Casassa, S.; Baima, J.; Salustro, S.; Kirtman, B. Quantum-Mechanical Condensed Matter Simulations with CRYSTAL. *Wiley Interdiscip. Rev. Comput. Mol. Sci.* **2018**, *8* (4), e1360.

(54)   Desmarais, J. K.; Erba, A.; Dovesi, R. Generalization of the Periodic LCAO Approach in the CRYSTAL Code to G-Type Orbitals. *Theor. Chem. Acc.* **2018**, *137* (2), 28.

(55)   El-Kelany, K. E.; Ravoux, C.; Desmarais, J. K.; Cortona, P.; Pan, Y.; Tse, J. S.; Erba, A. Spin Localization, Magnetic Ordering, and Electronic Properties of Strongly Correlated Ln$_2$O$_3$ Sesquioxides (Ln=La, Ce, Pr, Nd). *Phys. Rev. B* **2018**, *97* (24), 245118.

(56)   Bastow, T. J.; Stuart, S. N. ^{17}O NMR in Simple Oxides. *Chem. Phys.* **1990**, *143* (3), 459–467.

(57)   Kentgens, A. P. M. A Practical Guide to Solid-State NMR of Half-Integer Quadrupolar Nuclei with Some Applications to Disordered Systems. *Geoderma* **1997**, *80* (3–4), 271–306.

(58)   Florian, P.; Massiot, D.; Humbert, G.; Coutures, J. P. Etude Par RMN de ^{17}O et ^{89}Y Des Formes C et B de l'oxyde d'Yttrium Y$_2$O$_3$. *Comptes Rendus Académie des Sciences - Serie II*. 1995, pp 99–104.

(59)   Profeta, M.; Benoit, M.; Mauri, F.; Pickard, C. J. First-Principles Calculation of the ^{17}O NMR Parameters in Ca Oxide and Ca Aluminosilicates: The Partially Covalent Nature of the Ca−O Bond, a Challenge for Density Functional Theory. *J. Am. Chem. Soc.* **2004**, *126* (39), 12628–12635.

(60)   White, J. A.; Van Vleck, J. H. Sign of Knight Shift in Samarium Intermetallic Compounds. *Phys. Rev. Lett.* **1961**, *6* (8), 412–413.

(61)   Grey, C. P.; Cheetham, A. K.; Dobson, C. M. Temperature-Dependent Solid-State ^{119}Sn MAS

NMR of $Nd_2Sn_2O_7$, $Sm_2Sn_2O_7$, and $Y_{1.8}Sm_{0.2}Sn_2O_7$. Three Sensitive Chemical-Shift Thermometers. *J. Magn. Reson. Ser. A* **1993**, *101* (3), 299–306.

(62) Clark, S. J.; Segall, M. D.; Pickard, C. J.; Hasnip, P. J.; Probert, M. J.; Refson, K.; Payne, M. C. First Principles Methods Using {CASTEP}. *Z. Krist.* **2005**, *220*, 567–570.

(63) Kim, J.; Middlemiss, D. S.; Chernova, N. A.; Zhu, B. Y. X.; Masquelier, C.; Grey, C. P. Linking Local Environments and Hyperfine Shifts: A Combined Experimental and Theoretical ^{31}P and ^{7}Li Solid-State NMR Study of Paramagnetic Fe(III) Phosphates. *J. Am. Chem. Soc.* **2010**, *132* (47), 16825–16840.

(64) Clément, R. J.; Pell, A. J.; Middlemiss, D. S.; Strobridge, F. C.; Miller, J. K.; Whittingham, M. S.; Emsley, L.; Grey, C. P.; Pintacuda, G. Spin-Transfer Pathways in Paramagnetic Lithium Transition-Metal Phosphates from Combined Broadband Isotropic Solid-State MAS NMR Spectroscopy and DFT Calculations. *J. Am. Chem. Soc.* **2012**, *134* (41), 17178–17185.

(65) Lee, J.; Seymour, I. D.; Pell, A. J.; Dutton, S. E.; Grey, C. P. A Systematic Study of ^{25}Mg NMR in Paramagnetic Transition Metal Oxides: Applications to Mg-Ion Battery Materials. *Phys. Chem. Chem. Phys.* **2017**, *19* (1), 613–625.

(66) Campbell, G. C.; Crosby, R. C.; Haw, J. F. ^{13}C Chemical Shifts Which Obey the Curie Law in CP/MAS NMR Spectra. The First CP/MAS NMR Chemical-Shift Thermometer. *J. Magn. Reson.* **1986**, *69* (1), 191–195.

(67) Shannon, R. D. Revised Effective Ionic Radii and Systematic Studies of Interatomic Distances in Halides and Chalcogenides. *Acta Crystallogr. Sect. A* **1976**, *32* (5), 751–767.

(68) Levitt, M. H. *Spin Dynamics: Basics of Nuclear Magnetic Resonance*, 2nd ed.; John Wiley & Sons: Chichester, 2008.

(69) Fuda, K.; Kishio, K.; Yamauchi, S.; Fueki, K. Study on Vacancy Motion in Y_2O_3-Doped CeO_2 by ^{17}O NMR Technique. *J. Phys. Chem. Solids* **1985**, *46* (10), 1141–1146.

(70) Kim, N.; Hsieh, C.; Huang, H.; Prinz, F.; Stebbins, J. High Temperature ^{17}O MAS NMR Study of Calcia, Magnesia, Scandia and Yttria Stabilized Zirconia. *Solid State Ionics* **2007**, *178* (27–28), 1499–1506.

(71) Adler, S. B.; Smith, J. W. Effects of Long-Range Forces on Oxygen Transport in Yttria-Doped Ceria: Simulation and Theory. *J. Chem. Soc. Faraday Trans.* **1993**, *89* (16), 3123–3128.